ADVANCING EARTH AND SPACE SCIENCES

JGR Atmospheres

RESEARCH ARTICLE
10.1029/2025JD044140

Special Collection:
Extreme Hydrometeorological Events Under Climate Change: Past, Present, and Future

When Rain Meets Surge: Assessing Future Typhoon-Driven Compound Flood Hazard Profiles in a Rapidly Urbanizing Delta

Yu Li[1], Qinghua Ye[2], Jianhui Wei[1], Joël Arnault[1], Hanqing Xu[3,4,5], Qiaodan Liu[6], Zhan Tian[7,8], Laixiang Sun[9,10], Harald Kunstmann[1,11], and Patrick Laux[1,11]

[1]Institute of Meteorology and Climate Research (IMK-IFU), Karlsruhe Institute of Technology, Garmisch-Partenkirchen, Germany, [2]Deltares, Delft, The Netherlands, [3]Institute of Eco-Chongming (IEC), East China Normal University, Shanghai, P.R. China, [4]Key Laboratory of Geographic Information Science (Ministry of Education), School of Geographic Science, East China Normal University, Shanghai, P.R. China, [5]Institute for National Safety and Emergency Management, East China Normal University, Shanghai, P.R. China, [6]Faculty of Architecture and the Built Environment, Delft University of Technology, Delft, The Netherlands, [7]School of Environmental Science and Engineering, Southern University of Science and Technology, Shenzhen, P.R. China, [8]Peng Cheng Laboratory, Shenzhen, P.R. China, [9]Department of Geographical Sciences, University of Maryland, College Park, MD, USA, [10]School of Finance & Management, SOAS University of London, London, UK, [11]Institute of Geography, University of Augsburg, Augsburg, Germany

Key Points:

- By 2100, coastal water level (CWL) rise alone will intensify Shenzhen's typhoon flood hazard more than increased rainfall under SSP5-8.5
- The combined effects of rainfall and CWL increase medium-to-high risk area (inundation depth above 27 cm) by over 5%
- Flood hazards respond non-proportionally to rainfall and CWL perturbations

Supporting Information:

Supporting Information may be found in the online version of this article.

Correspondence to:

Y. Li,
yu.li@kit.edu

Citation:

Li, Y., Ye, Q., Wei, J., Arnault, J., Xu, H., Liu, Q., et al. (2026). When rain meets surge: Assessing future typhoon-driven compound flood hazard profiles in a rapidly urbanizing delta. *Journal of Geophysical Research: Atmospheres*, *131*, e2025JD044140. https://doi.org/10.1029/2025JD044140

Received 22 APR 2025
Accepted 21 JAN 2026

Author Contributions:

Conceptualization: Yu Li, Qinghua Ye, Joël Arnault, Zhan Tian, Laixiang Sun, Harald Kunstmann, Patrick Laux
Data curation: Yu Li, Jianhui Wei
Formal analysis: Yu Li, Qinghua Ye, Zhan Tian, Laixiang Sun, Harald Kunstmann, Patrick Laux
Funding acquisition: Zhan Tian, Laixiang Sun, Harald Kunstmann, Patrick Laux

Abstract Typhoon-induced Compound Flood (TCF), driven by the combined impact of extreme rainfall and increasing coastal water level (CWL), poses a substantial threat to urban safety. This study presents a framework for assessing the future compound flood hazard profiles in a coastal megacity in the Delta region of southern China. A coupled hydrology-hydrodynamic model is applied to simulate the flooding processes of 7 typhoon events. Scenarios are constructed using all possible pairwise combinations of three rainfall and three CWL conditions. These inputs are derived from statistical and dynamical downscaling of climate projections from the Coupled Model Intercomparison Project (CMIP6) ensemble under the SSP5-8.5 pathway. The results show that future CWL rise contributes more to future inundation than increasing rainfall, whereas rainfall contributions exhibit considerable uncertainties due to regional rainfall downscaling. Under extreme warming scenarios, future typhoons may produce increases of up to 230 mm in total rainfall and 28 mm per hour in rainfall intensity, which in turn increase the average urban inundation depth and area by 1.2 cm and 24.7 km^2, respectively. Given an average CWL of 170 cm and a maximum CWL of 440 cm in the future, the inundation depth and area could increase by up to 8.4 cm and 29 km^2, respectively. Within the 7 typhoons in this study, Hagupit (2014) exhibits the most notable compound effect, potentially expanding the medium-to-high risk area (inundation depth above 27 cm) by over 5%. This study demonstrates that climate change may intensify TCF, requiring flood-mitigating measures to consider rainfall-CWL interactions.

Plain Language Summary Typhoons are strong tropical storms that can cause higher coastal water levels and heavy rain, leading to floods in coastal cities. This study uses advanced simulation methods to predict inundation profiles during typhoons by the end of this century for a large coastal town under global warming conditions. It found that rising sea levels might have a bigger impact on future flooding than rainfall changes. Future typhoons in extreme warming conditions could bring up to 230 mm of rain, increasing by 28 mm per hour, raising flood depth by 1.2 cm, and spreading flooded areas by 25 km^2. Rising sea levels during typhoons could add 8 cm to flood depth and expand flooded areas by 29 km^2. When both heavy rain and rising sea levels occur, inundation height and extent increase remarkably. Typhoon Hagupit shows the strongest compound effect. These findings stress the need for specific actions to protect coastal cities from the combined threats of rain and sea-level rise.

1. Introduction

As climate extremes intensify, coastal cities are becoming progressively more vulnerable to compound flood events, driven by the simultaneous or sequential occurrence of heavy rainfall and elevated coastal water levels (CWLs) (Hendry et al., 2019; Nasr et al., 2021; Tao et al., 2022). Typhoons, as dominant meteorological systems in the North Pacific area, epitomize this synergy, delivering intense rainfall, storm surges, and wind-driven waves that collectively exacerbate inundation (Wu et al., 2025; Yan et al., 2024). Typhoon-induced Compound Flood

Investigation: Yu Li, Qiaodan Liu, Zhan Tian
Methodology: Yu Li, Qinghua Ye, Jianhui Wei, Joël Arnault, Hanqing Xu, Zhan Tian, Laixiang Sun, Harald Kunstmann, Patrick Laux
Project administration: Zhan Tian, Laixiang Sun, Harald Kunstmann, Patrick Laux
Resources: Yu Li, Qinghua Ye, Zhan Tian, Patrick Laux
Software: Yu Li, Qinghua Ye, Jianhui Wei, Joël Arnault, Hanqing Xu, Qiaodan Liu
Supervision: Qinghua Ye, Harald Kunstmann, Patrick Laux
Validation: Yu Li, Qinghua Ye, Jianhui Wei, Joël Arnault
Visualization: Yu Li, Hanqing Xu, Patrick Laux
Writing – original draft: Yu Li
Writing – review & editing: Qinghua Ye, Jianhui Wei, Joël Arnault, Hanqing Xu, Qiaodan Liu, Zhan Tian, Laixiang Sun, Harald Kunstmann, Patrick Laux

(TCF) represents one of the most critical and complex hazards in subtropical coastal regions, where the interplay between discharge, precipitation, and CWL leads to highly nonlinear and destructive flood dynamics. Densely populated delta megacities like Shanghai, Hong Kong, and Shenzhen are particularly susceptible to and have been widely documented to experience TCF (Lai et al., 2023; Xu et al., 2022).

Climate change adds a layer of complexity to TCF. According to the long-term records, 2015 to 2024 is the warmest decade, causing extreme weather to impact communities and economies worldwide (World Meteorological Organization (WMO), 2024). Compared with the historical period (1981–2010), mean and extreme precipitation over southern China is projected to increase substantially by the end of the century (2071–2100) (Liang & Haywood, 2023). Global mean Sea Level Rise (SLR) might amount to 65 ± 12 cm relative to 2005 by 2100 (Nerem et al., 2018). Along the China coast, projections under a 1.5°C warming scenario indicate a median SLR of 38–49 cm, relative to the 1986–2005 average (Qu et al., 2020). In addition, SLR is likely to increase tidal ranges in estuaries with dampened tidal regimes (Khojasteh et al., 2023). However, while we expect these TCF drivers to shift in response to warming, especially rainfall intensification and SLR, we currently lack robust quantitative estimates of how evolving typhoon characteristics will shape compound flood hazards.

To overcome this limitation, various methodologies have been developed for assessing future compound flood hazards. Typically, within these frameworks, future extreme event projections focus on changes in frequency and intensity, addressing how return periods for specific intensities will change (Shepherd, 2016). In the case of compound flooding, multiple contributing factors are involved, necessitating a joint statistical treatment (Bevacqua et al., 2017; Jalili Pirani & Najafi, 2023; Latif & Simonovic, 2022). Such future risk analyses typically rely on long-term climatological simulations. For example, Hermans et al. (2024) and Bermúdez et al. (2021) developed a methodological framework to assess changes in compound flooding under climate change scenarios based on outputs from Coupled Model Intercomparison Project (CMIP6) climate models. Notably, a series of statistical-dynamical downscaling approaches for rapidly estimating tropical cyclone tracks and precipitation have also proven effective for future TCF assessment (Santiago-Collazo et al., 2021; Sarhadi et al., 2024). A complementary framework to risk-based attribution is the storyline approach, which is defined as a physically self-consistent unfolding of past or plausible future events or pathways (Shepherd et al., 2018). The storyline approach avoids the deep uncertainty inherent in long-term simulated dynamics by addressing the question: *For given historically impactful typhoon events, how do projected climate changes affect the magnitude of the resulting compound flood hazard?* An example is given in Goulart et al. (2024), developing spectrally nudged storylines of Hurricane Sandy to evaluate the compound flooding impacts on critical infrastructure in New York City.

The Pseudo-Global Warming (PGW) approach is an efficient, computationally cost-effective method for constructing storylines related to extreme weather events (Schär et al., 1996; Xue et al., 2023). The core idea of PGW is to directly impose large-scale changes in the climate system onto a control regional climate simulation, typically representing present-day conditions, by modifying the boundary conditions (Brogli et al., 2023). In regional climate modeling research, the PGW approach is widely adopted for simulating extreme meteorological events under climate change (Grimley et al., 2024; Heim et al., 2023; Lackmann, 2015; Olschewski et al., 2024). Further validation comes from Tanaka et al. (2023), which shows that the PGW experiments and the risk-based approach yield consistent basin-averaged accumulated rainfall in all target basins, underscoring the robustness of the PGW method for extreme event assessments.

Extreme events, such as high-impact typhoons, provide critical input for long-term policy formulation and hazard mitigation planning. However, only a few studies estimate future TCF in Shenzhen (Bai et al., 2023) despite its higher population density and increased TCF exposure over the past four decades.

To fill this gap, our previous work focused on assessing the potential impact of climate change on typhoon intensity using the Weather Research & Forecasting (WRF) model, following a PGW-based storyline approach (Olschewski et al., 2024). In this study, we expand upon this work to simulate the flooding from these typhoon realizations using a coupled hydrology-hydrodynamic model, taking modeled WRF rainfall and CWLs from Deltares Global Tide and Surge Model version 3.0 (GTSM3.0) as boundary conditions. We aim to quantify the contributions of future changes in rainfall and CWL to compound flooding under the SSP5-8.5 scenario. Particular emphasis is given on evaluating the responses of these two drivers to climate warming and assessing their impacts on flood depth, the dominant mechanism, and the compound effects.

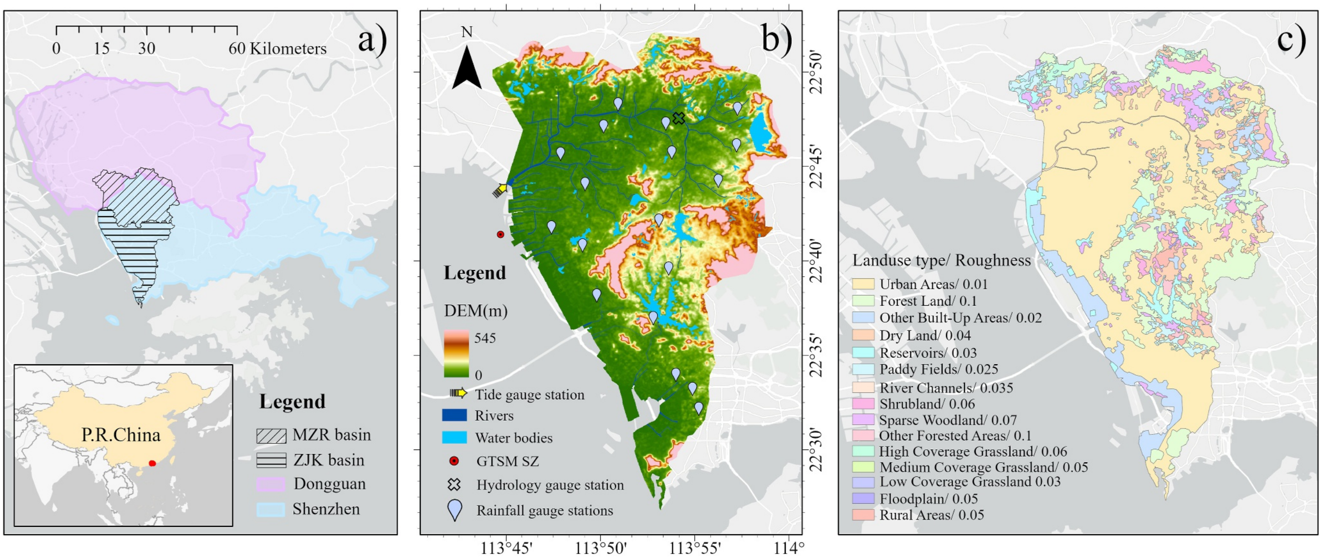

Figure 1. Details of the research area: (a) Location, (b) the elevation and gauge station locations, and (c) the land-use types and the Manning's roughness coefficient assigned in the hydrodynamic model.

2. Research Area and Data Sets

2.1. Research Area

Shenzhen, a coastal metropolis with a population of more than 17 million (Shenzhen Statistics Bureau, 2021), is located in the economically developed and densely populated Pearl River Delta in southern China. Shenzhen has a subtropical monsoon climate, with an average annual rainfall of approximately 1,930 mm during the most recent climate normal period (1991–2020), from which 86% of the annual precipitation occurs during the rainy season, which stretches from April to September. Shenzhen is prone to severe weather events, including frequent typhoons in summer and occasional autumn typhoons in certain years (Shenzhen Meteorological Bureau, 2024).

The research area's location, terrain, and land use are shown in Figure 1. The total area of Shenzhen is 1987 km^2; the whole region can be divided into 9 hydrological subbasins. The hydrodynamic model is constructed for the Maozhou River Basin (MZR) and the Zhujiangkou Basin (ZJK), which cover 670 km^2. The MZR spans the border between Shenzhen and Dongguan and features a primary stream running approximately 31 km east to west toward the sea, with tributaries spread throughout the basin. Situated in the western coastal region of Shenzhen, the ZJK contains several minor drainage channels that flow into the sea. ZJK is highly susceptible to flood risks because of its expansive, low-lying coastal regions (Bai et al., 2023). Since the launch of China's reform and opening-up policy, Shenzhen has undergone rapid urbanization in the past few decades. As observed in the selected study areas, urban regions dominate the landscape. As urbanized areas substantially overlap with low-lying regions, urban areas are highly vulnerable to TCF.

2.2. Typhoon Case Selection

To maintain consistency with previous research by Olschewski et al. (2024) on typhoon simulation using the PGW method, this study utilizes the same typhoon cases. These cases were selected based on the performance of the WRF model in reproducing maximum wind speed and minimum sea level pressure, making them typical typhoons affecting Shenzhen and enabling a robust investigation of warming-induced intensity changes. Besides, typhoon Mangkhut was chosen for model calibration due to its high impact (Section 2.1) and extensive gauge data. The paths of 8 typhoons are depicted in Figure 2, including the distance from their landing points to the research area, as well as their intensity upon landing. Most of these typhoons moved from the southeast to the northwest, except typhoon Neoguri, which traveled from the south to the north.

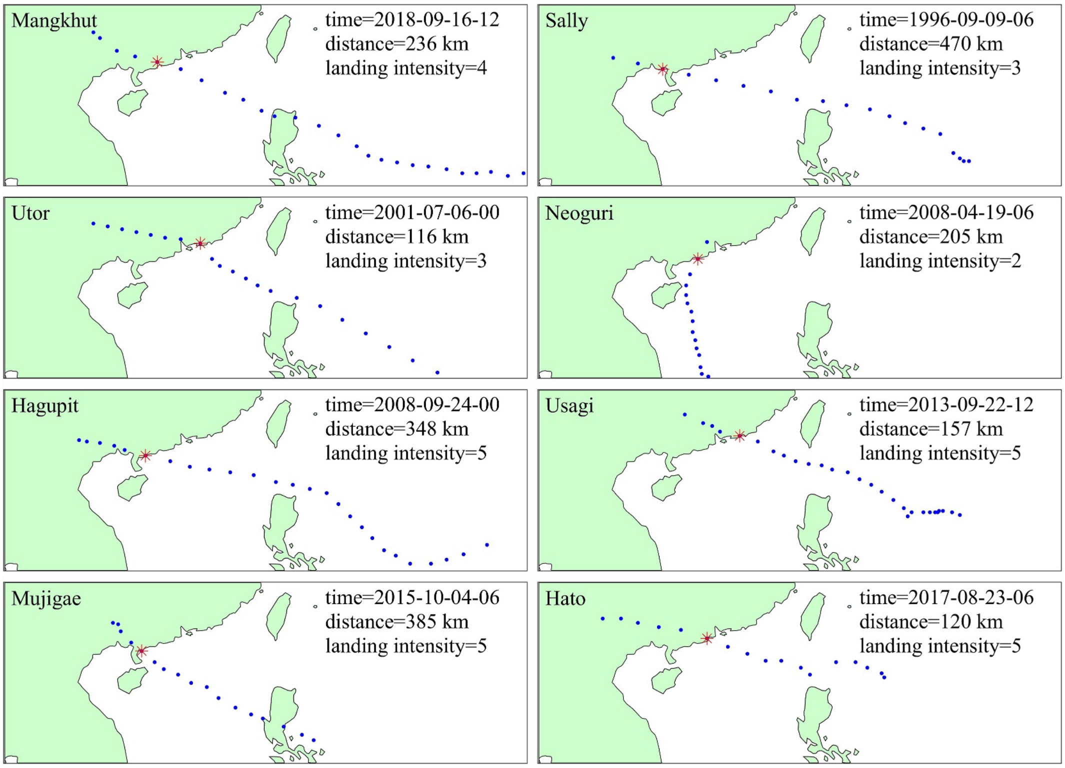

Figure 2. Typhoon tracks for typhoon Mangkhut and another 7 selected typhoon cases. The blue dots are 6-hr intervals. Red stars mark each track's closest point to the coastline, with corresponding time, distance to the research area, and intensity displayed in the upper right corner.

2.3. Data Sets

The rainfall data are derived from WRF downscaling combined with the PGW method (Olschewski et al., 2024), with the driving data from CMIP6 scenarios (Eyring et al., 2016). The hourly rainfall data for calibration and validation are obtained from the Shenzhen Meteorological Bureau. The CWL data for future scenarios are from the Copernicus data set and are produced by a Deltares-led consortium including Vrije Universiteit Amsterdam, IHE Delft on behalf of the Copernicus Climate Change Service (Muis et al., 2022). The hourly gauge discharge and tidal data are from Huadong Engineering Corporation Limited. The static geographical data of the research area, including elevation, land use types, and river channel data, are also from Huadong Engineering Corporation Limited. The sparse waterlogging data come from the Water Authority of Bao'an District, Shenzhen Municipality. The gauge data sets of tide, discharge, waterlogging observations, and static data are not publicly released.

3. Methods

3.1. Calibration and Projection Model Frameworks

To investigate the compound flood driven by rainfall and CWLs, we design an integrated modeling framework as illustrated in Figure 3a. The WRF model is used to downscale the ERA5 reanalysis data and climate fields perturbed with GCM-derived temperature anomalies, producing historical and future regional rainfall fields. The Delft3D Flexible Mesh Suite (D-FLOW FM) supports both inland inundation modeling (D-FLOW 1D2D) and GTSM3.0, using separate meshes for inland and ocean regions. D-FLOW 1D2D simulates 1D and 2D hydrodynamic processes within the inland region. It is fully coupled with D-Rainfall Runoff, which models rainfall-runoff processes across sub-catchments. Meanwhile, GTSM3.0 simulates CWLs, accounting for tides, storm surges, and sea-level rise on decadal scales, as well as their interactions.

In D-Rainfall Runoff, each sub-catchment is divided into paved and unpaved areas to simulate hydrological processes in urbanized and natural land surfaces separately. This lumped hydrological model is bidirectionally

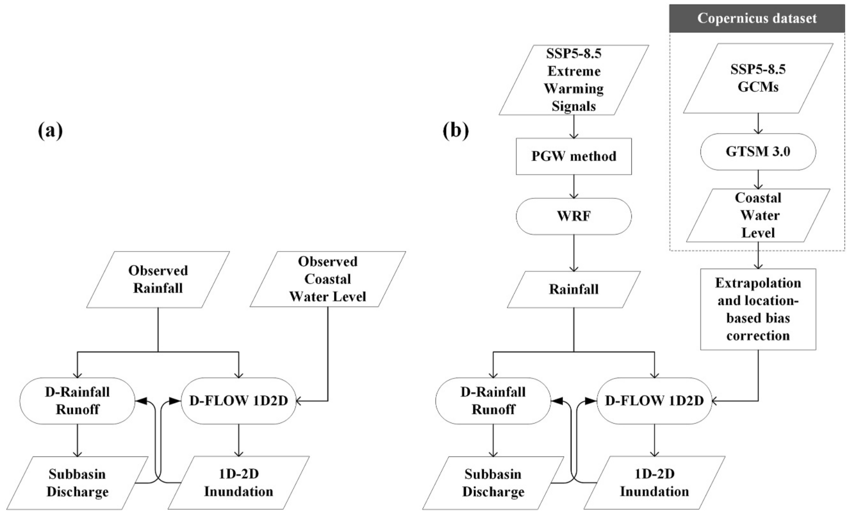

Figure 3. The processes of (a) the model calibration framework for the typhoon Mangkhut event, and (b) the model framework for historical and future scenarios for the selected 7 typhoons.

coupled to a node within the 1D hydrodynamic model, enabling the exchange of water level and flow dynamics. Each node in the 1D hydrodynamic model is further bidirectionally coupled with a 2D hydrodynamic cell, thereby achieving full two-way coupling among hydrology, 1D hydrodynamics, and 2D hydrodynamics. GTSM3.0 provides CWL conditions, which are directly passed to the hydrodynamic model as input boundary conditions for the coastal region. This integrated modeling framework enables us to comprehensively analyze the compound impacts of rainfall and CWLs on urban flooding in the study region. For model calibration, the rainfall and CWL data are replaced by observed data to control the uncertainty from the boundary conditions and to test the efficiency of the hydrology and hydrodynamic models. The model framework is depicted in Figure 3b.

3.2. Projected Scenarios of Typhoon Rainfall

To project and downscale rainfall scenarios under warming conditions in the future, the PGW method is applied within the WRF model by modifying the boundary conditions in the historical period with warming signals (Olschewski et al., 2024). The warming signals are derived from the mean difference between the temperature in the future period (2071–2100) and the historical period (1985–2014). The two thermodynamically-based storylines used in this study present favorable and unfavorable conditions for typhoon intensification, respectively. Specifically, the former storyline pairs the maximum SST warming with the minimum atmospheric warming, while the latter pairs the smallest SST warming with the largest atmospheric warming. In the following, these two scenarios are referred to as hiS-loA and loS-hiA, respectively.

For the downscaling experiments, the WRF model (version 4.3.3) is used. WRF has been used to simulate typhoon events and is reported to have good reliability (Dong et al., 2021; Jiang et al., 2023; Skamarock et al., 2019). In this study, a nested approach is followed to downscale the meteorological forcing from a resolution of 0.25° to 25 km in the outer domain (d01) and 5 km in the inner domain (d02), with a temporal resolution of 1 hr. Both domains use an uneven vertical division of 52 levels up to 50 hPa. Spectral nudging adjusts the typhoon tracks to historical data by influencing horizontal wind speeds above the 500 hPa level every 6 hr, aligning them with ERA5 data without affecting the typhoon's inner core (Storch et al., 2000).

3.3. Processing Coastal Water Level

GTSM3.0 is an unstructured barotropic model based on the Delft3D FM software developed by Deltares (Muis et al., 2020). GTSM3.0 has global coverage and, therefore, has no open boundaries, which makes the model very flexible to apply to different settings or for different scenarios. GTSM3.0 can be run in tide-only, surge-only, or combined tide-surge mode, optionally including sea-level rise. In this way, interaction effects between tides, storm surges, and mean sea level can be included.

10.1029/2025JD044140

Table 1
Relative CWL Rise in cm Between the Year of the Typhoons and 2100 for the 5 GCMs

GCMs	Typhoons and periods						
	Sally 1996-	Utor 2001-	Neoguri 2008-	Hagupit 2008-	Usagi 2013-	Mujigae 2015-	Hato 2017-
CMCC-CM2-VHR4	57.4	53.2	53.4	53.4	51.8	54.7	52.6
EC-Earth3P-HR	81.5	77.3	77.5	77.5	76.0	78.9	76.7
GFDL-CM4C192-SST	61.1	56.9	57.2	57.2	55.6	58.5	56.4
HadGEM3-GC31-HM	78.6	74.4	74.6	74.6	73.0	75.9	73.8
HadGEM3-GC31-HM-SST	71.7	67.5	67.7	67.7	66.2	69.0	66.9

The Copernicus data set provides the historical reanalysis of CWLs and future projected CWLs derived from five GCMs under the high-emission scenario SSP5-8.5 (Muis et al., 2022). Due to limited CWL observations in Shenzhen, the reanalysis CWLs are used to represent the historical baseline. The reanalysis CWLs are adjusted using available observations from 8 June 2016, to 5 October 2019. Figure 3b refers to this process as extrapolation and location-based bias correction. The details are as follows: Shenzhen ST2 (Figure 1 as GTSM3.0 SZ) is the closest simulation output point to the tide gauge station. We used the relationship between the observed CWL data set from the tide gauge station (Figure 1) to post-process the model output from Shenzhen ST2. After a distance-based adjustment, the CWL is in good agreement with the observed values, and the first-order regression coefficient is close to 1 (Figure S1 in Supporting Information S1).

Subsequently, a quadratic regression model is fitted to the CWL rise signals from five GCMs, which is then used for extrapolation to evaluate CWL rise signals (Figure S2 in Supporting Information S1). The rise in CWL signals between the years of typhoons and 2100 for the 5 GCMs is shown in Table 1. The CMCC-CM2-VHR4 has the lowest CWL rise signals, while EC-Earth3P-HR produces the highest CWL rise signals; the other three are in between. In this study, we select the CMCC-CM2-VHR4 and EC-Earth3P-HR outputs to represent the most moderate and the most extreme scenarios of future CWL, respectively. In the following, they are abbreviated as w1 and w2. The reanalysis CWLs after adjustment are used as the historical reference, abbreviated as w0.

3.4. Hydrological Processes in the Sub-Basins of the Maozhou River

The D-Rainfall Runoff is a module compliant with the Delta Shell framework, which is designed to simulate rainfall-runoff processes (Prinsen et al., 2010). It supports multiple modeling concepts, including the polder concept, Sacramento, and Hydrologiska Byråns Vattenbalansavdelning, with the polder concept specifically developed for low-lying areas. This concept represents the area as a bucket model, balancing water inflows and outflows to simulate hydrological processes in rural and urban settings under varying conditions. Key processes modeled include rainfall, evaporation, surface runoff, infiltration, and drainage. The modeling concept is lumped, which means that there is no direct interaction between the individual buckets. The module can operate independently or integrate with the D-FLOW 1D module for simultaneous or sequential calculations (Deltares, 2023).

In the study region, most of the rivers in the Pearl River Estuary basin directly discharge into the open sea and are controlled by CWLs rather than rainfall-runoff processes. Therefore, we only conducted hydrological zoning and calibration for the Maozhou River basin. For typhoon Mangkhut, there are sufficient hydrological and tidal data, so we used the period of Mangkhut for model calibration and validation. There was also extreme rainfall before Mangkhut, but the storm surge phenomenon was not obvious. We also included this period in our simulation. The details of calibration based on typhoon Mangkhut can be in Supporting Information S1 (Figures S3 and S4). As part of the model preprocessing and validation, simulations for periods during and before Mangkhut both reach a Nash-Sutcliffe Efficiency of 0.8, demonstrating that the hydrological component reproduces the observed discharge well.

3.5. Flood Modeling

D-FLOW FM is the integrated modeling system of Deltares for the aquatic environment. It uses a flexible mesh consisting of a combination of rectilinear or curvilinear cells and unstructured cells composed of triangles and/or quads, which allows for local cell refinement in areas with large horizontal gradients. In D-FLOW FM, the non-

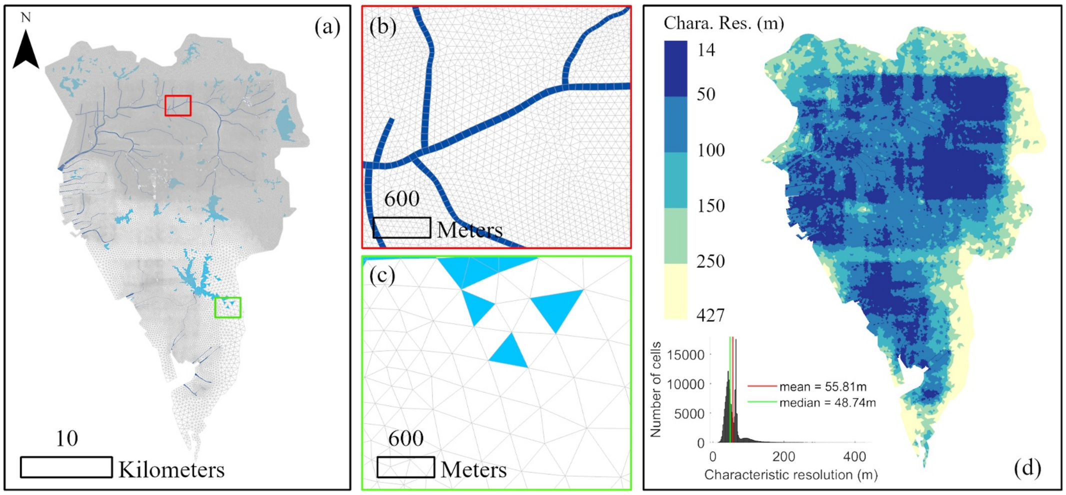

Figure 4. The two-dimensional unstructured hydrodynamic computational cells covering the study region are shown in (a). Zoom-in of an urban area of higher resolution is shown in (b), and a mountainous area with lower resolution is shown in (c). The resolution of all cells is shown in (d). The characteristic resolution is defined as the side length of an equal-area square.

linear shallow water equations are solved. The equations are derived from the three-dimensional Navier-Stokes equations for incompressible free surface flow under the shallow water and Boussinesq assumptions (Deltares, 2023). D-FLOW FM has been shown to exhibit excellent performance in simulating water levels in estuarine regions as part of a coupled model framework, with skill scores ranging from 0.79 to 0.91 near the storm peaks and negligible phase errors (Bakhtyar et al., 2020). In a comparative study, it was found that D-FLOW FM enhanced with atmospheric forcing predicts total water levels more accurately and 6 to 10 times faster than the 2D HEC-RAS model (Muñoz et al., 2022). Furthermore, D-FLOW FM has already been applied to assess compound flood and shows good performance (Ke et al., 2021; Xu et al., 2024).

D-FLOW 1D2D is applied in this study to simulate the hydrodynamic processes of the region without considering depth-dependent variations. Unstructured cells are applied to cover the entire study region (Figure 4a), with different resolutions employed in urban (Figure 4b) and mountainous regions (Figure 4c) to balance computational efficiency and accuracy requirements. The entire region consists of 173,541 cells, with cell characteristic resolution sizes ranging from 14 to 427 m. The characteristic resolution is defined as the side length of an equal-area square or as the square root of the cell area (Figure 4d). The mean characteristic resolution of the cells is 55.8 m, and the median value is 48.7 m. For the river channel and its adjacent floodplain, where the wetting-drying transition might occur, we apply mesh refinement to minimize sharp topographic gradients that can lead to artificial spikes in inundation depth.

The original elevation data, with a resolution of 30 m (Figure 1b), are first interpolated to the center of each computational cell using the inverse distance weighting method to obtain the cell elevations. Subsequently, the elevations of the major rivers' channel cells are manually adjusted based on their locations, shown on Google Maps and surveyed cross-sectional data. The Manning's roughness coefficient of each computational cell depends on the land-use type shown in Figure 1d; the roughness assigned for each land-use type is marked in the legend. Then the roughness is assigned to computational cells based on their geographical location. A 1 cm depth threshold distinguished wet and dry cells during the simulation.

Similar to the hydrological model, the hydrodynamic model is evaluated during typhoon Mangkhut and its associated pre-typhoon heavy rainfall events, with corresponding inundation maps provided in Figure S5 in Supporting Information S1. The results of these two periods can reflect the model's ability to capture the different flooding patterns. The model can be used for further quantitative assessments of inundation profiles under changing climate conditions.

Table 2
Experiment Design

Experiment	Boundary conditions (Rain + CWL)
1	Reanalysis + w0
2	Reanalysis + w1
3	Reanalysis + w2
4	loS-hiA + w0
5	loS-hiA + w1
6	loS-hiA + w2
7	hiS-loA + w0
8	hiS-loA + w1
9	hiS-loA + w2

3.6. Experiment Design and Metrics Definition

The experiments are shown in Table 2, and the input rainfall and CWLs for 7 typhoons are shown in Figure 5. The hydrometeorological conditions from the reanalysis are used as baseline reference, referred to as Reanalysis for Rain and w0 for CWL. By taking all possible pairwise combinations of the three rainfall inputs, Reanalysis, hiS-loA, and loS-hiA, and three CWLs, w0, w1, and w2, we obtain an ensemble of 9 members for further hydrodynamic modeling. The ensemble subsets of the members using Renalysis, hiS-loA, and loS-hiA are called ENS(Reanalysis), ENS(hiS-loA), and ENS(loS-hiA), respectively. The ensemble subsets of the members using w0, w1, and w2 are called ENS(w0) and ENS(w1), and ENS(w2), respectively.

We calculate several key metrics to quantify the flood drivers. After removing the area of permanent water bodies, the remaining 627 km^2 is used for all subsequent inundation calculations, including as the denominator for the inundation ratio. For rainfall, the domain-averaged hourly rain rate $\left(\bar{R}_t\right)$ is computed across the WRF grids. This is then used to derive the total storm rainfall (R_{tot}) by summing the hourly means over the typhoon period, and the maximum hourly rainfall $(R_{\max})$ as the peak of the hourly mean series. Similarly, the characteristics of the CWL input are quantified by the average CWL $\left(\bar{L}\right)$ and the maximum CWL $(L_{\max})$ during the typhoon period. The hydrodynamic model output is analyzed using two primary hazard metrics: inundation area (A_{inu}) and average inundation depth $\left(\bar{D}_{\text{inu}}\right)$.

The isolated impact of CWL and Rainfall on flooding is referred to as a single-factor effect, which takes the maximum of the outputs from the experiments using maximum CWL alone (with rainfall using Reanalysis) and maximum rainfall alone (with CWL using w0). The combined impact of CWL and Rainfall on flooding is referred to as a dual-factor effect, which directly takes the results from the experiment using maximum CWL and Rainfall together. The compound effect depth (D_{comp}) is defined as the difference between the dual-factor inundation depth and the single-factor inundation depth. The mathematical definitions for these averages and the compound effect are detailed in Supporting Information S1. The original plan for calculating the single-factor effect is to take the maximum inundation for each computational cell from experiments 3 and 7 and then evaluate the corresponding metrics. However, because the experiment with the maximum rainfall output differed across typhoon cases, the final calculation applied a filter selecting the case with the largest R_{tot} from Experiments 1, 4, and 7. The equations of the above variables and metrics can be found in Supporting Information S1.

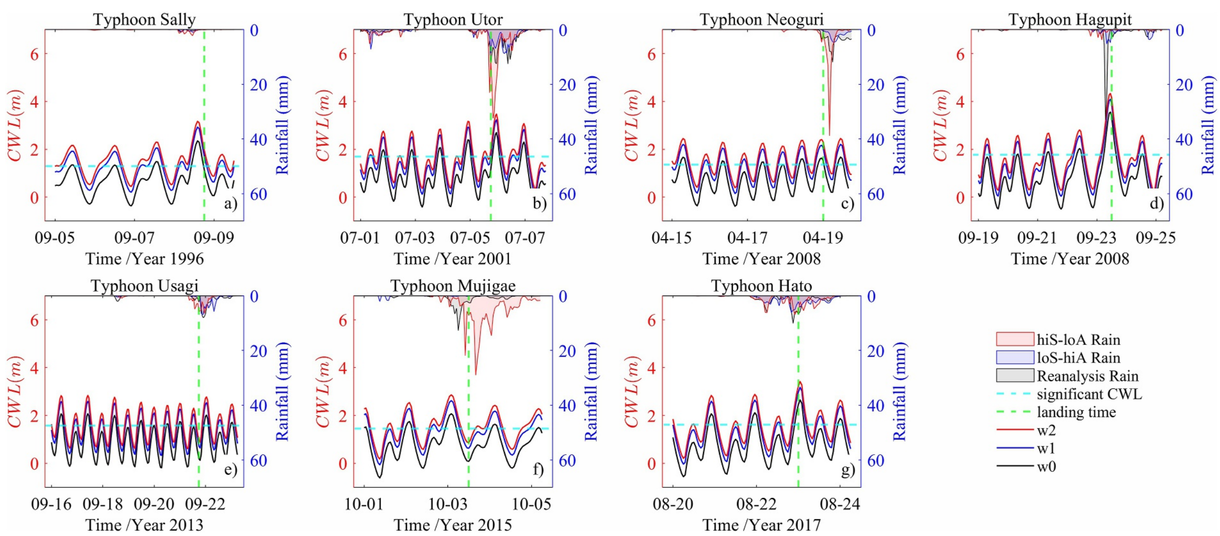

Figure 5. Input rainfall and coastal water level boundary conditions for 7 typhoons.

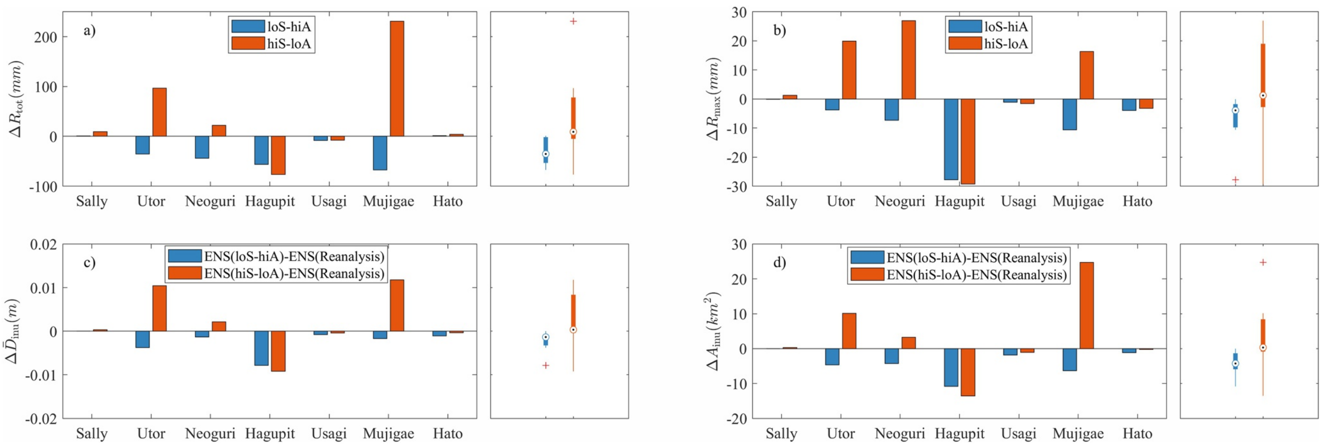

Figure 6. (a) Difference in total rainfall compared to Reanalysis. (b) Difference in maximum rainfall compared to Reanalysis. (c) Difference in average inundation depth of ENS(hiS-loA) and ENS(loS-hiA) compared to ENS(Reanalysis). (d) Difference in inundated area of ENS(hiS-loA) and ENS(loS-hiA) compared to ENS (Reanalysis).

We follow the classification scheme from the Beijing Urban Waterlogging and Flood Risk Map released by the Beijing Municipal Water Authority in 2024 (with thresholds of 15, 27, and 40 cm representing low, medium, and high risk, respectively), using A_{MHR} to indicate the area of inundation depth greater than 27 cm, which corresponds to medium-to-high risk in this case (Beijing Municipal Water Authority, 2024).

4. Results

4.1. Rainfall-Attributed Flood Hazard Profiles

Figures 6c and 6d illustrates the changes in inundation metrics when only the rainfall input is altered. Across the 7 typhoon cases under the hiS-loA scenario, the average increase in $\bar{D}_{inu}$ is 0.2 cm, with $\bar{A}_{inu}$ increasing by 3.4 km^2. The largest increases are 1.2 cm in $\bar{D}_{inu}$ and 24.7 km^2 in $\bar{A}_{inu}$ (typhoon Mujigae). Whereas under loS-hiA scenario, both $\bar{D}_{inu}$ and $\bar{A}_{inu}$ decreased to varying degrees.

The change of inundation metrics tend to be more responsive to fluctuations in the R_{max} (Figure 6). However, once R_{tot} exceeds a certain threshold, both $\bar{D}_{inu}$ and $\bar{A}_{inu}$ become more strongly influenced by R_{tot} than by R_{max}. For instance, in the hiS-loA scenario during typhoon Neoguri, the R_{max} increased substantially by 28 mm (Figure 6b), an increase larger than those observed during typhoons Utor and Mujigae; yet, the resulting increases in $\bar{D}_{inu}$ and A_{inu} were smaller than those during the latter two events. This lack of a clear, linear relationship between changes in rainfall metrics and inundation outcomes, particularly where R_{tot} increases but $\bar{D}_{inu}$ decreases (e.g., during typhoon Hato). Although R_{tot} may have increased, a more evenly spread distribution across time or space could yield a lower intensity at any given point, thereby reducing the resulting inundation and contributing to the observed complexity.

To illustrate this uncertainty in rainfall downscaling, the spatial distributions of accumulated rainfall for 7 typhoons are plotted. The figure for typhoon Hagupit is shown in Figure 7, and the rest is in the SI material (Figures S6–S11 in Supporting Information S1). Figure 7 shows that in the hiS-loA scenario, the accumulated rainfall within the WRF inner domain is notably greater than in the other two scenarios, with enhanced rain on both sides of the track. However, the subplots in the upper-right corner show that rainfall over the Shenzhen area is actually lower than in the other two cases. This difference helps explain the results in Figure 6. Unlike most typhoon events, Hagupit under the hiS-loA scenario does not show an increase in rainfall. As a result, both the total and the maximum rainfall in the study region are smaller than those in the reanalysis and loS-hiA scenarios. Based on the accumulated rainfall spatial patterns alone, it appears that rainfall during the late stage of Hagupit's life cycle decreased substantially in the hiS-loA scenario compared with the other two (Figures 6a, 6b, and 6d).

Overall, for most typhoon events, the loS-hiA scenario, which is less favorable for typhoon formation, results in decreases in R_{tot} and R_{max}, thereby reducing $\bar{D}_{inu}$ and $\bar{A}_{inu}$. In contrast, the hiS-loA scenario demonstrates the

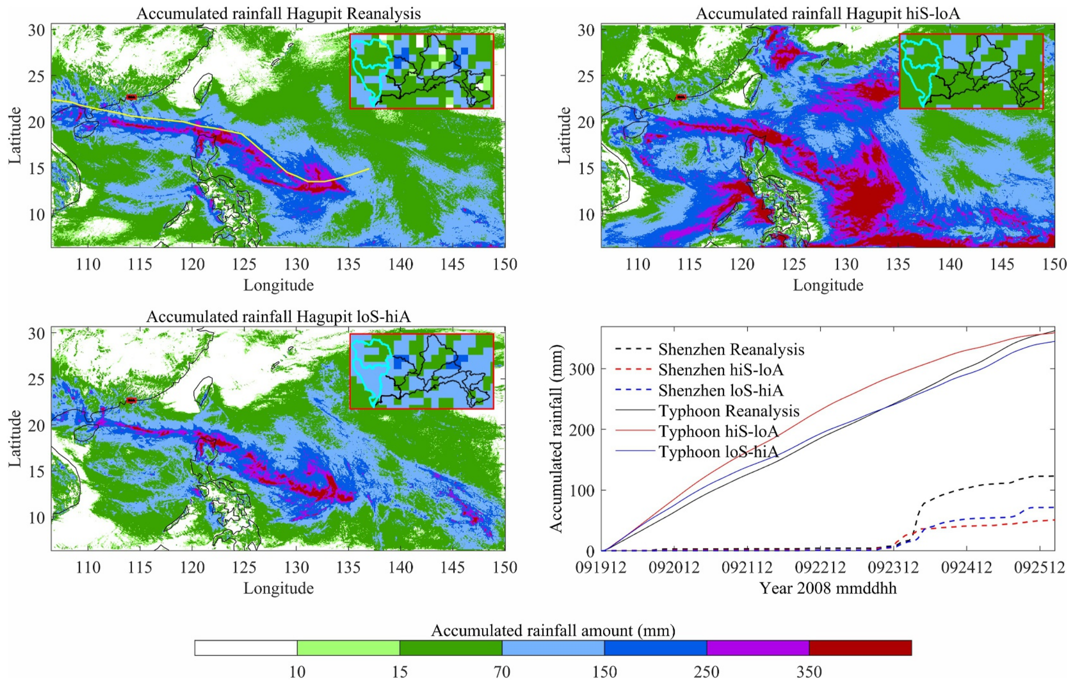

Figure 7. Accumulated rainfall distribution and time series during typhoon Hagupit, with an inset at the upper right of the panel showing a magnification of Shenzhen and the cyan area represents the hydrodynamic modeling extent. (a) Spatial distribution of accumulated rainfall in the WRF inner domain during typhoon Hagupit based on reanalysis data; (b) Same as (a) but for the hiS-loA scenario; (c) Same as (a) but for the loS-hiA scenario; (d) Comparison of hourly accumulated rainfall time series. Solid lines in (d) indicate accumulation within a 500 km radius from the hourly typhoon center, while dashed lines correspond to accumulation within the Shenzhen area. The yellow line in panel (a) indicates the best typhoon track provided by the Hong Kong Observatory.

opposite pattern. Furthermore, compared to loS-hiA, rain in the 7 typhoon cases under hiS-loA exhibits a higher range of uncertainty. When translated into inundation simulation results, this uncertainty becomes more pronounced. Moreover, our results suggest that both $R_{\max}$ and R_{tot} are important for assessing flooding and that considering only one metric could lead to misattribution.

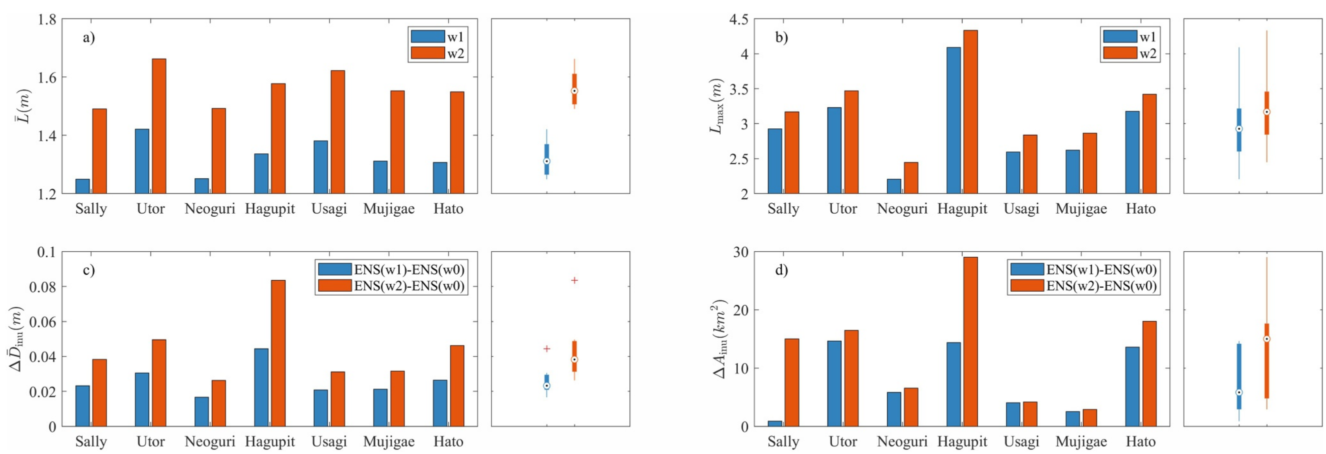

Figure 8. (a) Average of coastal water level (CWL) input, (b) Maximum of CWL input, (c) Difference in average inundation depth of ENS(w1) and ENS(w2) compared to ENS(w0). (d) Difference in inundation area of ENS(w1) and ENS(w2) compared to ENS(w0).

Table 3
Increase in the Area of Inundation Greater Than 27 cm Due To Compound Effects

Typhoon	Single-factor (km^2)	Dual-factor (km^2)	Added area (km^2)	Added percentage
Sally	38.34	38.34	0	0
Utor	64.20	64.91	0.70	1.09%
Neoguri	39.58	39.63	0.05	0.12%
Hagupit	81.31	85.72	4.41	5.42%
Usagi	38.73	38.75	0.02	0.04%
Mujigae	45.71	45.76	0.05	0.11%
Hato	53.73	54.04	0.31	0.57%

4.2. CWL-Attributed Flood Hazard Profiles

Figures 8c and 8d illustrates the changes in inundation metrics when only the CWL is altered. Across all scenarios, the increase in CWL consistently leads to a substantial increase in both $\bar{D}_{\text{inu}}$ and A_{inu}. Under w1 and w2 boundary conditions, $\bar{D}_{\text{inu}}$ increases from 1.7 to 4.5 cm (w1) and 2.6 to 8.4 cm (w2), while A_{inu} expands from 0.9 to 14.7 km^2 (w1) and 2.9 to 29 km^2 (w2). Changes in L_{max} show a more consistent tendency to coincide with variations in $\bar{D}_{\text{inu}}$ and A_{inu} than changes in $\bar{L}$. This suggests that under conditions such as typhoon storm surges or extreme rain, the deepest inundation in coastal or estuarine regions typically occurs during (or approaches) the L_{max} phase, while the $\bar{L}$ appears insufficient to fully capture the dominant impact of flood or tidal waters during the most critical periods. Across the 7 typhoon cases under w2, the average increase in $\bar{D}_{\text{inu}}$ is 4.4 cm, with A_{inu} increasing by 13.2 km^2. The largest increases are 8.4 cm in $\bar{D}_{\text{inu}}$ and 29 km^2 in $\bar{A}_{\text{inu}}$ (typhoon Hagupit).

Notably, some typhoon cases deviate from this trend. For example, during typhoon Sally, the CWLs under the w1 scenario were much higher than those observed for Neoguri, Usagi, and Mujigae, yet the corresponding A_{inu} was smaller than that of the latter three. This phenomenon is likely related to coastal topography or protective structures, as well as the duration of high CWLs: the longer high CWL persists, the more time low-lying areas have to become fully inundated, thereby expanding the inundation area. In gently sloping areas, there is usually a linear relationship between L_{max} and the maximum inundation extent, whereas in areas with steep terrain, increases in CWL may result in little change in the inundation area until a certain threshold is exceeded, at which point the inundation area can suddenly increase.

4.3. Compound Effect Contribution

In the former two sections, we evaluate the contributions of rainfall and CWL to urban flooding. The findings indicate that flood response is not the simple additive of the two individual effects. This finding aligns with previous studies, which also emphasize the compound nature of flood processes (Bilskie & Hagen, 2018; Gori et al., 2020; Grimley et al., 2025). Therefore, following the analysis of single-factor impacts, we now proceed to assess the compound effects of CWL and rainfall on coastal flooding during the 7 typhoons.

Table 3 illustrates the increase in D_{inu} greater than 27 cm due to compound effects across 7 typhoons. The compound effect increases the A_{MHR} in every typhoon. The largest increase, 5.4%, is observed during typhoon Hagupit, whereas the smallest, 0, is observed during typhoon Sally. A consistent pattern of increase with the single-factor A_{MHR} is observed: the larger the single-factor A_{MHR}, the more pronounced the ΔA_{MHR}, and vice versa. The exacerbating inundation due to the interaction between rainfall and CWL is observed in almost all 7 typhoons, presenting more substantial challenges for urban flood prevention and control. It is noted that to ensure the compound effect case represents the strongest potential combined impact, the selection described in Section 3.6 may result in cases such as typhoon Hagupit, where the spatial pattern of D_{comp} is large while the $\bar{D}_{\text{inu}}$ and A_{inu} are negative (Figures 6c and 6d). A further result is that for grid cells where rainfall in the loS-hiA scenario exceeds that in hiS-loA and Reanalysis, D_{comp} can be negative (Figure S12 in Supporting Information S1).

The spatial distribution of D_{comp} is shown in Figure 9. Positive values indicate a deeper inundation resulting from the compound effect, whereas negative values show a reduced inundation depth. A threshold of 1 cm is used to determine whether the compound effect is notable. It shows that in most typhoon events, the compound effect

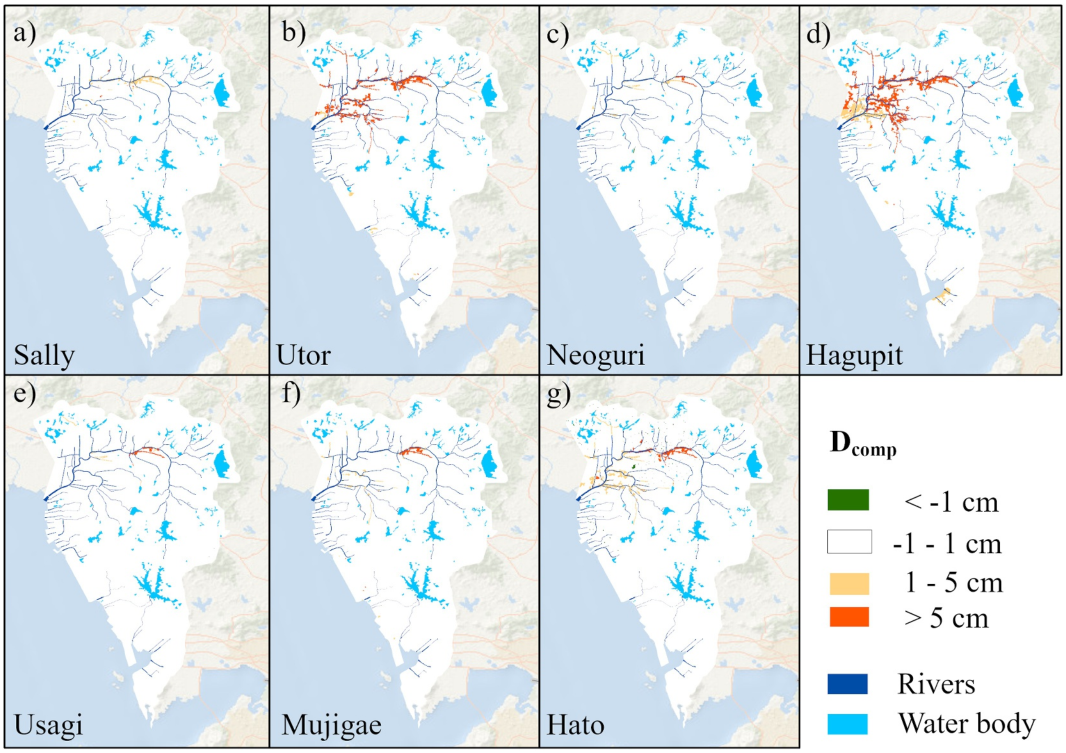

Figure 9. Increased inundation depth caused by the compound effect of 7 typhoons. Subpanels (a–g) present results from individual simulations for each of the 7 typhoons.

leads to greater D_{max}. The most pronounced effects are found along the mainstream of the Maozhou River, extending into the mid-reaches. When the overall compound effect is strong, the mid-reaches are typically more affected than the downstream areas; this is because downstream inundation is mainly driven by CWL, while upstream inundation is primarily influenced by rainfall and runoff, and their interaction converges in the mid-reaches. In addition, the low-lying terrain near the mainstream monitoring station of the Maozhou River is particularly sensitive to the compound effect. Although certain areas near the drainage channels of the Pearl River Estuary also experience impacts, D_{comp} they generally do not exceed 5 cm.

Table 4 provides further details on the area experiencing increases in D_{inu} due to the compound effect: for typhoon Hagupit, D_{comp} is above 1 cm across 35 km^2 and above 5 cm across 24 km^2, corresponding to 5.5% and 3.8% of the total area. In other typhoon events, an area of about 5–22 km^2 experiences an increase of D_{inu} above 1 cm, and 0.14–19 km^2 experiences an increase of D_{inu} above 5 cm. Overall, these results highlight the critical role of compound effects between rainfall and CWL in shaping urban flood profiles under future climate change scenarios.

Table 4
Compound Effect Depth During 7 Typhoons

Typhoon	Area of D_{comp} >1 cm (km^2)	Area of D_{comp} >5 cm (km^2)
Sally	4.67	0.14
Utor	22.21	19.27
Neoguri	6.11	1.24
Hagupit	35.12	24.08
Usagi	4.68	2.76
Mujigae	10.11	2.33
Hato	17.23	5.03

5. Discussion

The discussion centers around the changes in typhoon rainfall and coastal water levels, followed by the regional controls of flood drivers. We then discuss the uncertainties arising from typhoon characteristics and the downscaling approach. Finally, the limitations of this study are outlined.

5.1. Projected Changes and Regional Controls of Flood Drivers

Under climate change, rainfall projections for 7 typhoons from our experiments show opposing trends in the two scenarios: the hiS-loA scenario increases R_{tot} by up to 231 mm, while the loA-hiS scenario decreases it by up to 67 mm (Figures 6a and 6b). For the CWL, increases of about 77.9 and 53.8 cm

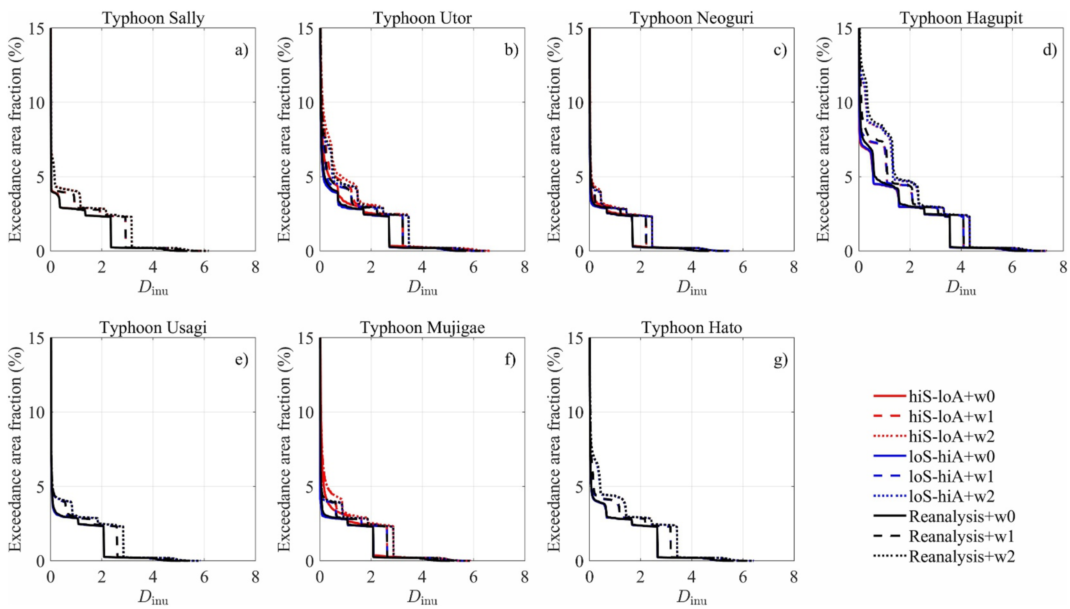

Figure 10. Exceedance area curve of inundation depth during 7 typhoons under nine experiments. Subpanels (a–g) present result for each of the 7 typhoons.

are assigned to scenarios w1 and w2 across 7 typhoons (Table 1). Our analysis reveals that changes in flood drivers (i.e., modified rainfall or CWL) do not yield a proportional change in the resulting hazard metrics (inundation depth and area). The non-linear compound flooding effect was also illustrated by the compound flood research in New York city (Sarhadi et al., 2024). This non-proportional response underscores the complex interactions inherent in compound flooding systems, reinforcing the necessity of using fully coupled hydrodynamic models to accurately capture the hazard cascade, as highlighted by recent reviews of Green et al. (2025). By linking changes in the climate state (PGW) through atmospheric physics (WRF) to local impact (D-FLOW FM), our framework addresses the need to balance global-to-local models with varying spatial and temporal resolutions, ensuring a physically self-consistent hazard assessment, particularly in situations of deep uncertainty.

Due to differences in geomorphology and hydrometeorological conditions, the dominant factors driving compound flooding vary across different regions globally (Eilander et al., 2020). To clarify the flood-generation characteristics of our study region, we further examined D_{inu} exceedance area curves (Figure 10). The exceedance area curves highlight that deep inundation in the study region is primarily controlled by CWLs, while rainfall mainly modulates the extent of shallow flooding. Several abrupt drops in the curves indicate that large parts of the domain share similar inundation depths. The rightmost x-axis intersections reflect a small fraction (around 2.5%) of the area with extremely high inundation depth, which may be associated with reclaimed coastal land that remains at very low elevation and is therefore highly sensitive to CWLs. Rainfall exerts a more spatially uniform effect, as seen in typhoon Utor, primarily modifying the depth and extent of shallow inundation.

Beyond topography, however, catchment characteristics such as flashiness, size, and elevation gradient (Harrison et al., 2021; Hendry et al., 2019), as well as weather systems (Couasnon et al., 2020), differ across regions and may influence the frequency of compound floods and the dependency on various drivers. Although these factors were not explicitly analyzed here, acknowledging their potential influence underscores the need for region-specific, integrated assessments in future work to better understand how compound flooding varies across regions.

5.2. Uncertainties From Typhoon Characteristics and Downscaling

Compared to previous studies that typically simulate only 1 to 3 typhoon events (Goulart et al., 2024; Koks et al., 2023; Wang et al., 2022; Yin et al., 2021), this study simulates 7 typhoons, primarily based on the availability of PGW simulation data. While the selection was not made by systematically controlling for all storm attributes, the resulting set of cases nonetheless spans a range of landfall timings, locations, and intensities. This diversity allows for preliminary exploration of how certain storm characteristics may influence compound flooding under future scenarios. Our results show that typhoon characteristics exert a stronger control on compound flooding intensity than climate change itself. For instance, Hagupit and Hato, both making landfall at intensity 5 near astronomical high tide (Figure 3), caused much more severe inundation than Usagi and Mujigae, which also made landfall at intensity 5 but during low tide. Similarly, Neoguri weakened to level 2 before landfall, leading to a smaller surge effect despite occurring near high tide. These findings align with Hendry et al. (2019), which also highlighted storm-specific meteorological features as key drivers of spatial variability in compound flooding.

In addition to typhoon characteristics, uncertainties also arise from the downscaling of rainfall and CWLs. Translating global phenomena like climate change to examine their local impacts inevitably involves uncertainties (Koks et al., 2023). The rainfall input in the future scenarios for inundation calculation in this study is downscaled by WRF. Even though the meteorological model captures an increase in rainfall in the typhoon-scale domain area during hiS-loA scenarios, the potential spatial mismatches in the rainfall input field will lead to an unstable rainfall tendency in our research area (Figure 7 and Figures S6–S11 in Supporting Information S1). Therefore, to capture changes in typhoon-induced rainfall, the downscaling errors within this study's modeling framework should be considered. This is also pointed out in the review of Chen et al. (2025) that finding a suitable resolution for the simulation of hydro-meteorological processes is still being debated. We conceive that achieving a balance between fine resolution and uncertainties from downscaling may merit greater attention and application in future research.

Future CWLs for each typhoon case are generated by adding a climate-change increment to the historical series. The extrapolation method used to extend CWL data sets is based on the assumption that the relationship between Shenzhen ST2 and the tide gauge station holds for all time periods under consideration. Although this increment considers various tidal components, potential storm surges, and future sea-level rise, the annual-scale calculations are likely to underestimate extreme CWL. Nevertheless, comparison with previous studies (Koks et al., 2023; Qu et al., 2020) suggests that our scenarios (w1 and w2) fall within the plausible range of 1.5°–2°C warming projections.

5.3. Limitations

The existing methods for analyzing and modeling compound events are highly diverse, relying on numerous subjective decisions, such as selecting compounding mechanisms and variables, defining a plausible hazard scenario, choosing a representative dependence model, and considering suitable temporal and spatial scales (Zscheischler et al., 2020). Our study provides a potential choice for the Shenzhen area, which is a combination of selected drivers, scenarios, models, and resolution. Nevertheless, there are still limitations to this study.

Many studies take a more optimistic view of climate change and suggest the world is presently on a lower emissions trajectory than is often assumed (Hausfather, 2025; Pielke et al., 2022), whereas this study only considers a high-impact warming scenario, that is, the SSP5-8.5. The CWL and rainfall used in this study are driven by the background under this extreme warming scenario, which may lead to an overestimation of future flood inundation.

Due to the lack of tide gauge data, the water level treatment might be simplistic. Only data from one gauge was available to calibrate the GTSM3.0 model output, which could affect the accuracy of the CWL. This aspect could be improved in future studies by employing Shenzhen's storm surge model to substitute GTSM3.0 interpolation results with higher-resolution CWL simulations. The local waterlogging observation during or after typhoons is also extremely scarce. In this study, the D-FLOW 1D2D model was calibrated using only one historical typhoon event, which means that the model parameters may not be fully applicable when transferred to other typhoon events. For example, urbanization and infrastructure development, as well as hydrological conditions, can vary over time. However, considering that typhoon-related flooding is quite extreme, the impact of these variables is comparatively limited.

Research indicates that human activities can also affect future flood risks and alter inundation patterns in the Pearl River Delta region (Zhang et al., 2025). Our research does not consider this effect and focuses only on natural flood drivers. However, the model framework provides the potential ability to incorporate planned infrastructure changes (e.g., seawalls, drainage improvements) to better estimate future flood risks in Shenzhen in the next steps.

6. Conclusions and Perspectives

In this study, we quantified the impacts of climate change on typhoon-induced compound flooding under the high-impact SSP5-8.5 scenario, building upon a PGW-based storyline approach. By integrating WRF-modeled rainfall and GTSM3.0-modeled coastal water levels (CWLs) into a coupled hydrology-hydrodynamic model, we evaluated the typhoon-induced inundation responses to these two key drivers under climate warming. Furthermore, our analysis quantified the non-proportional and combined impacts of rainfall and CWL on flood hazard profiles. Our main conclusions are:

1. By 2100, CWL rise alone will intensify Shenzhen's typhoon flood hazard more than increased rainfall under SSP5-8.5. The change in these drivers does not yield a proportional change in the hazard. Under the hiS-loA warming scenario, which is favorable for typhoon intensification, total storm rainfall may increase by up to 230 mm compared to the reanalysis, and maximum hourly rainfall may increase by up to 28 mm. This, in turn, could lead to an increase in average inundation depth to 1.2 cm and an increase in inundation area to 24.7 km^2. Under the highest CWL signal, w2 scenario, the average CWL may increase to 1.7 m, the maximum CWL may increase to 4.4 m, and the average inundation depth and inundation area may increase by 8.4 cm and 29 km^2, respectively.
2. The compound effects of CWLs and rainfall will exacerbate future typhoon-induced flooding. Typhoon Hagupit exhibits the most severe case among the 7 typhoons, while under compound effects, inundation depths increased by about 5 cm over more than 3.8% of the study area, and the medium-to-high risk area, with inundation depth above 27 cm, expanded by 5.4%.
3. The compound effects will cause deeper and wider flooding mainly in the middle and lower reaches of the watershed. The most pronounced effects are primarily found along the mainstream of the Maozhou River, extending into the mid-reaches.

Finally, we emphasize that the assessment of compound flooding is influenced by specific regional characteristics (such as topography and climate) and the inherent uncertainties propagated from the downscaling of drivers like rainfall and CWL. This highlights the need for coupled modeling approaches that can explicitly capture the interactions among the atmosphere, land, and coastal processes, thereby enabling a more physically consistent and region-specific evaluation of flood hazards.

Inclusion in Global Research Statement

This research was conducted in collaboration with researchers and institutions based in China; the field data used in this study were obtained with appropriate permissions from the Shenzhen Meteorological Bureau, Huadong Engineering Corporation Limited, and the Water Authority of Bao'an District. We acknowledge the assistance of local technicians who supported data acquisition.

Conflict of Interest

The authors declare no conflicts of interest relevant to this study.

Data Availability Statement

Data used in this study include sea level change time series from CMIP6 models provided by the Copernicus Climate Data Store (Muis et al., 2022), tropical cyclone best track data from the Hong Kong Observatory (Hong Kong Observatory, 2023), and atmospheric reanalysis data from ERA5 at both pressure levels (Hersbach et al., 2023a) and single levels (Hersbach et al., 2023b). All data sets are openly accessible from the corresponding repositories.

Acknowledgments

This work was supported by the project Research on the Mechanism of Responses via Multi-scale Interface Processes to Future Extreme Compound Flooding Risks in the Great Bay Area, funded by the National Natural Science Foundation of China (Grant 42430407). The study was conducted in the framework of the Sino-German project Mitigating the Risk of Compound Extreme Flooding Events, MitRiskFlood, jointly funded by MOST (Grant 2019YFE0124800) and the German Ministry of Education and Research (BMBF, Grant 01LP2005A). Y.L. is financially supported by the Chinese Scholarship Council (CSC). We thank the Copernicus Climate Change Service (C3S) and Deltares-led consortium, including Vrije Universiteit Amsterdam, IHE Delft for the public provision of Global sea level change time series. We also thank the Shenzhen Meteorological Bureau, Huadong Engineering Corporation Limited, and the Water Authority of Bao'an District for providing observed data sets and fundamental data of the research area. Open Access funding enabled and organized by Projekt DEAL.

References

Bai, P., Wu, L., Chen, Z., Xu, J., Li, B., & Li, P. (2023). Investigating the storm surge and flooding in Shenzhen City, China. *Remote Sensing*, *15*(20), 5002. https://doi.org/10.3390/rs15205002

Bakhtyar, R., Maitaria, K., Velissariou, P., Trimble, B., Mashriqui, H., Moghimi, S., et al. (2020). A new 1D/2D coupled modeling approach for a riverine-estuarine System under storm events: Application to Delaware River Basin. *Journal of Geophysical Research: Oceans*, *125*(9), e2019JC015822. https://doi.org/10.1029/2019JC015822

Beijing Municipal Water Authority. (2024). Beijing urban waterlogging and flood risk map. Retrieved from https://www.beijing.gov.cn/ywdt/zwzt/2024aqdx/xqfw/202406/t20240614_3712420.html

Bermúdez, M., Farfán, J. F., Willems, P., & Cea, L. (2021). Assessing the effects of climate change on compound flooding in coastal River areas. *Water Resources Research*, *57*(10), e2020WR029321. https://doi.org/10.1029/2020wr029321

Bevacqua, E., Maraun, D., Hobæk Haff, I., Widmann, M., & Vrac, M. (2017). Multivariate statistical modelling of compound events via pair-copula constructions: Analysis of floods in Ravenna (Italy). *Hydrology and Earth System Sciences*, *21*(6), 2701–2723. https://doi.org/10.5194/hess-21-2701-2017

Bilskie, M. V., & Hagen, S. C. (2018). Defining flood Zone transitions in low-gradient coastal regions. *Geophysical Research Letters*, *45*(6), 2761–2770. https://doi.org/10.1002/2018GL077524

Brogli, R., Heim, C., Mensch, J., Sørland, S. L., & Schär, C. (2023). The pseudo-global-warming (PGW) approach: Methodology, software package PGW4ERA5 v1.1, validation, and sensitivity analyses. *Geoscientific Model Development*, *16*(3), 907–926. https://doi.org/10.5194/gmd-16-907-2023

Chen, X., van der Werf, J. A., Droste, A., Coenders-Gerrits, M., & Uijlenhoet, R. (2025). Barriers to urban hydrometeorological simulation: A review. *Hydrology and Earth System Sciences*, *29*(15), 3447–3480. https://doi.org/10.5194/hess-29-3447-2025

Couasnon, A., Eilander, D., Muis, S., Veldkamp, T. I. E., Haigh, I. D., Wahl, T., et al. (2020). Measuring compound flood potential from river discharge and storm surge extremes at the global scale. *Natural Hazards and Earth System Sciences*, *20*(2), 489–504. https://doi.org/10.5194/nhess-20-489-2020

Deltares. (2023). D-flow flexible mesh user manual. Retrieved from https://content.oss.deltares.nl/delft3dfm2d3d/D-Flow_FM_User_Manual.pdf

Dong, W., Feng, Y., Chen, C., Wu, Z., Xu, D., Li, S., et al. (2021). Observational and modeling studies of oceanic responses and feedbacks to typhoons Hato and Mangkhut over the northern shelf of the South China Sea. *Progress in Oceanography*, *191*, 102507. https://doi.org/10.1016/j.pocean.2020.102507

Eilander, D., Couasnon, A., Ikeuchi, H., Muis, S., Yamazaki, D., Winsemius, H. C., & Ward, P. J. (2020). The effect of surge on riverine flood hazard and impact in deltas globally. *Environmental Research Letters*, *15*(10), 104007. https://doi.org/10.1088/1748-9326/ab8ca6

Eyring, V., Bony, S., Meehl, G. A., Senior, C. A., Stevens, B., Stouffer, R. J., & Taylor, K. E. (2016). Overview of the coupled model intercomparison project phase 6 (CMIP6) experimental design and organization. *Geoscientific Model Development*, *9*(5), 1937–1958. https://doi.org/10.5194/gmd-9-1937-2016

Gori, A., Lin, N., & Xi, D. (2020). Tropical cyclone compound flood hazard assessment: From investigating drivers to quantifying extreme water levels. *Earth's Future*, *8*(12), e2020EF001660. https://doi.org/10.1029/2020EF001660

Goulart, H. M. D., Benito Lazaro, I., van Garderen, L., van der Wiel, K., Le Bars, D., Koks, E., & van den Hurk, B. (2024). Compound flood impacts from Hurricane Sandy on New York City in climate-driven storylines. *Natural Hazards and Earth System Sciences*, *24*(1), 29–45. https://doi.org/10.5194/nhess-24-29-2024

Green, J., Haigh, I. D., Quinn, N., Neal, J., Wahl, T., Wood, M., et al. (2025). Review article: A comprehensive review of compound flooding literature with a focus on coastal and estuarine regions. *Natural Hazards and Earth System Sciences*, *25*(2), 747–816. https://doi.org/10.5194/nhess-25-747-2025

Grimley, L. E., Hollinger Beatty, K. E., Sebastian, A., Bunya, S., & Lackmann, G. M. (2024). Climate change exacerbates compound flooding from recent tropical cyclones. *npj Natural Hazards*, *1*(1), 1–10. https://doi.org/10.1038/s44304-024-00046-3

Grimley, L. E., Sebastian, A., Leijnse, T., Eilander, D., Ratcliff, J., & Luettich, R. (2025). Determining the relative contributions of runoff, coastal, and compound processes to flood exposure across the Carolinas during hurricane florence. *Water Resources Research*, *61*(3), e2023WR036727. https://doi.org/10.1029/2023WR036727

Harrison, L. M., Coulthard, T. J., Robins, P. E., & Lewis, M. J. (2021). Sensitivity of estuaries to compound flooding. *Estuaries and Coasts*, *45*(5), 1250–1269. https://doi.org/10.1007/s12237-021-00996-1

Hausfather, Z. (2025). An assessment of current policy scenarios over the 21st century and the reduced plausibility of high-emissions pathways. *Dialogues on Climate Change*, *2*(1), 32. https://doi.org/10.1177/29768659241304854

Heim, C., Leutwyler, D., & Schär, C. (2023). Application of the pseudo-global warming approach in a kilometer-resolution climate simulation of the tropics. *Journal of Geophysical Research: Atmospheres*, *128*(5), e2022JD037958. https://doi.org/10.1029/2022JD037958

Hendry, A., Haigh, I. D., Nicholls, R. J., Winter, H., Neal, R., Wahl, T., et al. (2019). Assessing the characteristics and drivers of compound flooding events around the UK coast. *Hydrology and Earth System Sciences*, *23*(7), 3117–3139. https://doi.org/10.5194/hess-23-3117-2019

Hermans, T. H. J., Busecke, J. J. M., Wahl, T., Malagón-Santos, V., Tadesse, M. G., Jane, R. A., & Van De Wal, R. S. W. (2024). Projecting changes in the drivers of compound flooding in Europe using CMIP6 models. *Earth's Future*, *12*(5), e2023EF004188. https://doi.org/10.1029/2023EF004188

Hersbach, H., Bell, B., Berrisford, P., Biavati, G., Horányi, A., Muñoz Sabater, J., et al. (2023a). Era5 hourly data on pressure levels from 1940 to present [Dataset]. *Copernicus Climate Change Service (C3S) Climate Data Store (CDS)*. https://doi.org/10.24381/cds.bd0915c6

Hersbach, H., Bell, B., Berrisford, P., Biavati, G., Horányi, A., Muñoz Sabater, J., et al. (2023b). Era5 hourly data on single levels from 1940 to present [Dataset]. *Copernicus Climate Change Service (C3S) Climate Data Store (CDS)*. https://doi.org/10.24381/cds.adbb2d47

Hong Kong Observatory. (2023). Tropical cyclone best track data (post analysis) [Dataset]. *Data.gov.hk*. Retrieved from https://data.gov.hk/en-data/dataset/hk-hko-rss-tropical-cyclone-best-track-data

Jalili Pirani, F., & Najafi, M. R. (2023). Characterizing compound flooding potential and the corresponding driving mechanisms across coastal environments. *Stochastic Environmental Research and Risk Assessment*, *37*(5), 1943–1961. https://doi.org/10.1007/s00477-022-02374-0

Jiang, C., Zhang, H., Gao, K., Yan, R., Lü, Z., & Wu, Z. (2023). Numerical investigation of the super typhoon mangkhut based on the coupled air-sea model. *Journal of Marine Sciences*, *41*(4), 21–31. http://hyxyj.sio.org.cn/EN/10.3969/j.issn.1001-909X.2023.04.003

Ke, Q., Yin, J., Bricker, J. D., Savage, N., Buonomo, E., Ye, Q., et al. (2021). An integrated framework of coastal flood modelling under the failures of sea dikes: A case study in shanghai. *Natural Hazards*, *109*(1), 671–703. https://doi.org/10.1007/s11069-021-04853-z

Khojasteh, D., Felder, S., Heimhuber, V., & Glamore, W. (2023). A global assessment of estuarine tidal response to sea level rise. *Science of The Total Environment*, *894*, 165011. https://doi.org/10.1016/j.scitotenv.2023.165011

Koks, E. E., Le Bars, D., Essenfelder, A., Nirandjan, S., & Sayers, P. (2023). The impacts of coastal flooding and sea level rise on critical infrastructure: A novel storyline approach. *Sustainable and Resilient Infrastructure*, *8*(sup1), 237–261. https://doi.org/10.1080/23789689.2022.2142741

Lackmann, G. M. (2015). Hurricane Sandy before 1900 and after 2100. *Bulletin of the American Meteorological Society*, *96*(4), 547–560. https://doi.org/10.1175/BAMS-D-14-00123.1

Lai, Y., Li, J., Chen, Y. D., Chan, F. K. S., Gu, X., & Huang, S. (2023). Compound floods in Hong Kong: Hazards, triggers, and socio-economic consequences. *Journal of Hydrology: Regional Studies*, *46*, 101321. https://doi.org/10.1016/j.ejrh.2023.101321

Latif, S., & Simonovic, S. P. (2022). Nonparametric approach to copula estimation in compounding the joint impact of storm surge and rainfall events in coastal flood analysis. *Water Resources Management*, *36*(14), 5599–5632. https://doi.org/10.1007/s11269-022-03321-y

Liang, J., & Haywood, J. (2023). Future changes in atmospheric rivers over East Asia under stratospheric aerosol intervention. *Atmospheric Chemistry and Physics*, *23*(2), 1687–1703. https://doi.org/10.5194/acp-23-1687-2023

Muis, S., Apecechea, M. I., Dullaart, J., de Lima Rego, J., Madsen, K. S., Su, J., et al. (2020). A high-resolution global dataset of extreme Sea levels, tides, and storm surges, including future projections. *Frontiers in Marine Science*, *7*, 263. https://doi.org/10.3389/fmars.2020.00263

Muis, S., Irazoqui Apecechea, M., Álvarez, J. A., Verlaan, M., Yan, K., Dullaart, J., et al. (2022). Global sea level change time series from 1950 to 2050 derived from reanalysis and high resolution cmip6 climate projections [Dataset]. *Copernicus Climate Change Service (C3S) Climate Data Store (CDS)*. https://doi.org/10.24381/cds.a6d42d60

Muñoz, D. F., Yin, D., Bakhtyar, R., Moftakhari, H., Xue, Z., Mandli, K., & Ferreira, C. (2022). Inter-Model comparison of Delft3D-FM and 2D HEC-RAS for total water level prediction in coastal to inland transition zones. *Journal of the American Water Resources Association*, *58*(1), 34–49. https://doi.org/10.1111/1752-1688.12952

Nasr, A. A., Wahl, T., Rashid, M. M., Camus, P., & Haigh, I. D. (2021). Assessing the dependence structure between oceanographic, fluvial, and pluvial flooding drivers along the United States coastline. *Hydrology and Earth System Sciences*, *25*(12), 6203–6222. https://doi.org/10.5194/hess-25-6203-2021

Nerem, R. S., Beckley, B. D., Fasullo, J. T., Hamlington, B. D., Masters, D., & Mitchum, G. T. (2018). Climate-change-driven accelerated sea-level rise detected in the altimeter era. *Proceedings of the National Academy of Sciences*, *115*(9), 2022–2025. https://doi.org/10.1073/pnas.1717312115

Olschewski, P., Sun, Q., Wei, J., Li, Y., Tian, Z., Sun, L., et al. (2024). A storyline-based approach towards changing typhoon intensities over the Pearl River Delta under future conditions using Pseudo-Global warming. *Hydrology and Earth System Sciences Discussions*, 1–32. https://doi.org/10.5194/hess-2024-95

Pielke, R., Jr., Burgess, M. G., & Ritchie, J. (2022). Plausible 2005–2050 emissions scenarios project between 2°C and 3°C of warming by 2100. *Environmental Research Letters*, *17*(2), 024027. https://doi.org/10.1088/1748-9326/ac4ebf

Prinsen, G., Hakvoort, H., & Dahm, R. (2010). Neerslag-afvoermodellering met SOBEK-RR. *Stormingen*, *15*(4), 8–24. http://refhub.elsevier.com/S0022-1694(24)00477-3/h0170

Qu, Y., Liu, Y., Jevrejeva, S., & Jackson, L. P. (2020). Future sea level rise along the coast of China and adjacent region under 1.5°C and 2.0°C global warming. *Advances in Climate Change Research*, *11*(3), 227–238. https://doi.org/10.1016/j.accre.2020.09.001

Santiago-Collazo, F. L., Bilskie, M. V., Bacopoulos, P., & Hagen, S. C. (2021). An examination of compound flood hazard zones for past, present, and future low-gradient coastal land-margins. *Frontiers in Climate*, *3*, 684035. https://doi.org/10.3389/fclim.2021.684035

Sarhadi, A., Rousseau-Rizzi, R., Mandli, K., Neal, J., Wiper, M. P., Feldmann, M., & Emanuel, K. (2024). Climate change contributions to increasing compound flooding risk in New York City. *Bulletin of the American Meteorological Society*, *105*(2), E337–E356. https://doi.org/10.1175/BAMS-D-23-0177.1

Schär, C., Frei, C., Lüthi, D., & Davies, H. C. (1996). Surrogate climate-change scenarios for regional climate models. *Geophysical Research Letters*, *23*(6), 669–672. https://doi.org/10.1029/96GL00265

Shenzhen Meteorological Bureau. (2024). Climate overview. Retrieved from http://weather.sz.gov.cn/qixiangfuwu/qihoufuwu/qihouguanceyupinggu/qihougaikuang/

Shenzhen Statistics Bureau. (2021). Shenzhen population census report. Retrieved from http://tjj.sz.gov.cn/zwgk/zfxxgkml/tjsj/tjgb/content/post_8771927.html

Shepherd, T. G. (2016). A common framework for approaches to extreme event attribution. *Current Climate Change Reports*, *2*(1), 28–38. https://doi.org/10.1007/s40641-016-0033-y

Shepherd, T. G., Boyd, E., Calel, R. A., Chapman, S. C., Dessai, S., Dima-West, I. M., et al. (2018). Storylines: An alternative approach to representing uncertainty in physical aspects of climate change. *Climatic Change*, *151*(3), 555–571. https://doi.org/10.1007/s10584-018-2317-9

Skamarock, C., Klemp, B., Dudhia, J., Gill, O., Liu, Z., Berner, J., et al. (2019). A description of the advanced research wrf model version 4. Retrieved from https://api.semanticscholar.org/CorpusID:196211930

Storch, H. v., Langenberg, H., & Feser, F. (2000). A spectral nudging technique for dynamical downscaling purposes. *Monthly Weather Review*, *128*(10), 3664–3673. https://doi.org/10.1175/1520-0493(2000)128<3664:asntfd>2.0.co;2

Tanaka, T., Kawase, H., Imada, Y., Kawai, Y., & Watanabe, S. (2023). Risk-based versus storyline approaches for global warming impact assessment on basin-averaged extreme rainfall: A case study for Typhoon Hagibis in eastern Japan. *Environmental Research Letters*, *18*(5), 54010. https://doi.org/10.1088/1748-9326/accc24

Tao, K., Fang, J., Yang, W., Fang, J., & Liu, B. (2022). Characterizing compound floods from heavy rainfall and upstream–downstream extreme flow in middle Yangtze River from 1980 to 2020. *Natural Hazards*, *115*(2), 1097–1114. https://doi.org/10.1007/s11069-022-05585-4

Wang, J., Mo, D., Hou, Y., Li, S., Li, J., Du, M., & Yin, B. (2022). The impact of typhoon intensity on wave height and storm surge in the northern east China sea: A comparative case study of typhoon muifa and typhoon lekima. *Journal of Marine Science and Engineering*, *10*(2), 192. https://doi.org/10.3390/jmse10020192

World Meteorological Organization (WMO). (2024). State of the Climate 2024. Retrieved from https://library.wmo.int/records/item/69075-state-of-the-climate-2024

Wu, L., Yu, R., Xiang, C., Yu, H., Feng, Y., & Zhou, X. (2025). Extreme impacts of four landfalling tropical cyclones in China during the 2024 peak season. *Advances in Atmospheric Sciences*, *42*(5), 817–824. https://doi.org/10.1007/s00376-025-4465-y

Xu, H., Ragno, E., Jonkman, S. N., Wang, J., Bricker, J. D., Tian, Z., & Sun, L. (2024). Combining statistical and hydrodynamic models to assess compound flood hazards from rainfall and storm surge: A case study of shanghai. *Hydrology and Earth System Sciences*, *28*(16), 3919–3930. https://doi.org/10.5194/hess-28-3919-2024

Xu, H., Tian, Z., Sun, L., Ye, Q., Ragno, E., Bricker, J., et al. (2022). Compound flood impact of water level and rainfall during tropical cyclone periods in a coastal city: The case of Shanghai. *Natural Hazards and Earth System Sciences*, *22*(7), 2347–2358. https://doi.org/10.5194/nhess-22-2347-2022

Xue, Z., Ullrich, P., & Leung, L.-Y. R. (2023). Sensitivity of the pseudo-global warming method under flood conditions: A case study from the northeastern US. *Hydrology and Earth System Sciences*, *27*(9), 1909–1927. https://doi.org/10.5194/hess-27-1909-2023

Yan, F., Shan, K., Zhao, H., & Yu, X. (2024). Growing threat of tropical cyclone disasters in inland areas of east China. *Geophysical Research Letters*, *51*(23), e2024GL111877. https://doi.org/10.1029/2024GL111877

Yin, K., Xu, S., Zhao, Q., Zhang, N., & Li, M. (2021). Effects of sea surface warming and sea-level rise on tropical cyclone and inundation modeling at Shanghai coast. *Natural Hazards*, *109*(1), 755–784. https://doi.org/10.1007/s11069-021-04856-w

Zhang, J., Yu, L., Sun, J., Liu, H., Ping, Y., Liu, Z., et al. (2025). Evaluating the influence of human activities on flood severity and its spatial heterogeneity across the pearl river delta. *Science of The Total Environment*, *960*, 178393. https://doi.org/10.1016/j.scitotenv.2025.178393

Zscheischler, J., Martius, O., Westra, S., Bevacqua, E., Raymond, C., Horton, R. M., et al. (2020). A typology of compound weather and climate events. *Nature Reviews Earth & Environment*, *1*(7), 333–347. https://doi.org/10.1038/s43017-020-0060-z